Pressure Pulsation Analysis of Oscillating Water Column Rotor Eccentricity Based on the Pulsation Tracking Network Method

J. Lu[1], Q. Liu[1], Z. Lu[1], R. Tao[1†], F. Jin[2], D. Zhu[3] and R. Xiao[1]

[1] *College of Water Resources and Civil Engineering, China Agricultural University, Beijing 100083, China*
[2] *Department of Energy and Power Engineering, Tsinghua University, Beijing 100084, China*
[3] *College of Engineering, China Agricultural University, Beijing 100083, China*

† Corresponding Author Email: randytao@cau.edu.cn

ABSTRACT

An oscillating water column (OWC) is typical of axial rotor turbines, which are used to convert ocean wave energy into electrical energy. This device impacts downstream pressure pulsations when its rotor becomes eccentric. This study compared the details of pressure pulsations downstream of eccentric and non-eccentric rotors under three operating conditions: low flow A, high-efficiency flow B, and high flow C. Computational fluid dynamics (CFD) simulations based on the pulsation tracking network (PTN) method were used for the OWC device to compare the experimental results. The results indicate downstream pressure pulsations were mostly dominated by the blade frequency in non-eccentric low-flow cases. In the other eccentric operating conditions, downstream pressure pulsations were mainly dominated by the 2-, 3.6-, 6-, and 7-times rotation frequencies and the 0.5-times blade frequency. The phase change of downstream pressure pulsations in eccentric and non-eccentric conditions is consistent with the flow direction. The phase change is relatively uniform and steady before eccentricity and becomes turbulent after eccentricity, which affects its steadiness. In this study, the OWC device did not significantly change with or without rotor eccentricity at a 1-time blade frequency intensity; however, at a 1-time rotation frequency, the OWC device showed a significant increase in the pressure pulsation amplitude after rotor eccentricity. The study of the dominant frequency, amplitude, and phase of pressure pulsations in OWC devices with eccentric rotors can help prevent excessive pressure pulsations that can lead to incidents.

1. INTRODUCTION

Seventy percent of the Earth's surface is covered by water, meaning that the oceans contain a huge amount of energy. With the continuous reduction in fossil energy, global warming, and ecological environmental deterioration, the energy crisis is becoming increasingly serious. Simshauser (2022). Therefore, ocean energy has great value for exploitation as a new type of clean energy (Pelc & Fujiata 2002). As one of the important manifestations of ocean energy, wave energy is utilized in a variety of ways due to its cyclical movement pattern. These include oscillating float wave energy converters, contracting wave channel wave energy converters, etc. Oscillating water column wave energy converters are widely used to allow these devices to operate safely and permanently in a constant direction of rotation, making the conversion of wave energy into electrical energy more sustainable (Kamath et al., 2015; Falcao & Henriques 2016).

At present, most air machines have the goal of becoming more efficient. To achieve this, the internal flow of the air machinery must be optimized, as blade tip leakage is one of the main causes of efficiency loss (Miorini et al., 2012). An OWC device is a typical air turbine, and blade tip leakage greatly affects its efficiency (Venter & Kroger 1992; Eric et al., 2022). When a pressure difference is created between the blade pressure surface and the suction surface, the fluid in the blade and shell gap meets the main flow, and a blade tip leakage vortex is formed (Gao et al., 2008; Decaix et al., 2018). A blade tip leakage vortex is a complex three-dimensional flow structure in the turbine rotor channel, and when the blade tip leakage is large enough, the vortex can dramatically affect the device's safe operation and power generation performance (Bell & He 2000; Rehder & Dannhauer 2007).

A specially designed rotor and stator are the core components of an OWC device. Due to the rotor's flexibility, it can become eccentric, and the center of rotation is off the cylinder's center if machining errors or

unbalanced forces occur (Wang 2004; Peters et al., 2007; Li et al., 2018). This results in uneven tip leakage, which disturbs the fluid movement downstream of the OWC device and significantly affects the efficiency of the OWC device. Uneven tip leakage generates additional radial excitation forces, which when increased to a certain value, destabilize the rotor and increase fluid energy losses near the blades (Wang et al., 2014a). If the excitation force reaches extreme values, it is likely to cause the rotor to collide with the shell, resulting in a safety accident (Bao et al., 2015). More importantly, the uneven blade tip leakage caused by eccentricity can change the local pressure pulsation amplitude downstream, which can affect the downstream fluid dominant frequency and disturb the phase stability propagation (Yu et al., 2022). considered the effect of impeller eccentricity due to parallel coupling misalignment and carried out a numerical study on the hydrodynamic characteristics of centrifugal pumps. The results showed that impeller eccentricity reduced the hydraulic performance of centrifugal pumps but had a small effect on the amplitude of the flow induction force at the rotation frequency (Wang et al., 2014b). speculated that uneven impeller end clearance in axial pumps may enhance flow noise and vibration in axial pumps. Therefore, they conducted numerical simulations of unsteady flow based on computational fluid dynamics for pumps with different eccentricity and flow discharges, and the results indicated that uneven vane end clearances caused multiple excitation forces to increase the pressure pulsation. Based on a tubular turbine model, Wang et al. (2022). explored in depth the Alford effect and Alford forces for different runner eccentricities using a combination of experiments and numerical simulations. The effect of the internal clearance flow field is the main cause of the Alford effect. Lu et al. (2022) used computational fluid dynamics equations to analyze the hydraulic performance and pressure pulsation in the bladeless region. The effect of the eccentric impeller on the hydraulic performance and pressure pulsation of each component was investigated. The results showed that the impeller eccentricity significantly increased the amplitude of the rotational frequency but had no significant effect on the blade passage frequency. Mao et al. (2016) analyzed the simulation of a centripetal turbine under steady eccentricity rate conditions based on the fast Fourier transform (FFT) using a simulation program and the effect of the rotor eccentricity on the excitation force. The results showed that the blades were subjected to approximately the same amplitude of the period and excitation forces in the X- and Y-axes. The FFT spectrum showed four independent frequencies located at 1X, 2X, 3X, and 4X, with the 3X component having a more pronounced fractional resonance. Based on the mathematical model of a single-span turbine rotor featuring initial bending and residual imbalance, Volokhovskaya & Barmina (2016). estimated the vibration amplitudes at the control points of the rotor span at speeds near the lowest critical values on the rundown (Sinha, 2002). realized machine state detection, comparing a practical truncated power series with autoregressive–moving-average methods for the trend prediction of steam turbines' vibration and eccentricity responses.

As the problem of pressure pulsation due to eccentricity in OWC devices has been less studied, this paper addressed this issue by combining computational fluid dynamics with pulsation tracking network methods to perform numerical simulations to compare and analyze the specific effects on an OWC device under eccentricity and non-eccentricity, including the pressure pulsation amplitude, principal frequency, and phase change, to reveal the details of its flow field variation. This is of great importance to improve the downstream pressure pulsation of an OWC device, increase the efficiency of the electrical energy conversion, and ensure the operation's safety, continuity, and stability.

2. RESEARCH OBJECTIVE

2.1 Oscillating Water Column Device

This paper focuses on the stator and rotor sections of an OWC device, which consists of an inlet section, an outlet section, an upstream and downstream stator, and a rotor. The upstream and downstream stators are symmetrical with respect to the rotor, which allows the OWC device to flow in both directions, but the rotor rotates in one direction. Thus, to simplify the analysis of the OWC equipment's motion, only the unidirectional flow case is considered in this study. The composition and gas flow direction of the OWC equipment are shown in Fig. 1.

The special designs of the rotor and stator are the key components of the energy conversion in the OWC device. As shown in Fig. 2, they are set up in the form of a blade, where the rotor has 30 blades, and the stator has 26. With this design, the airflow enters the rotor through the upstream stator and subsequently exits the downstream stator as shown in Fig. 2.
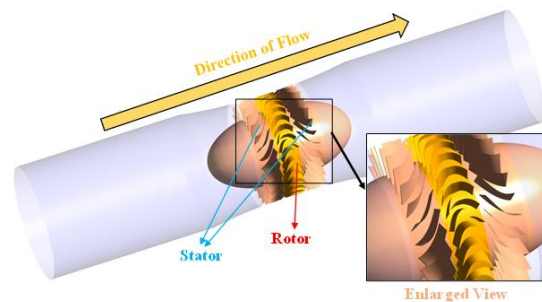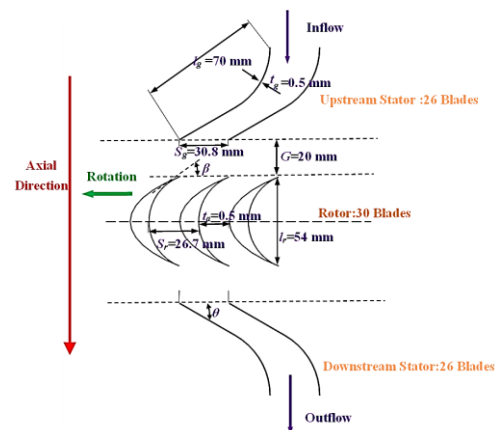

Fig. 1 Rotor and stator sections of OWC device

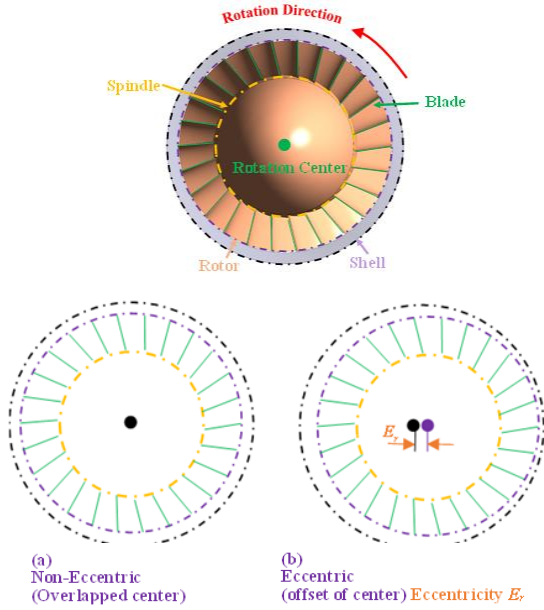**Fig. 2 Geometric parameters and profiles of rotor and stators**

Fig. 3 Eccentric and non-eccentric diagram

2.2 Rotor Eccentricity

This study addresses the analysis of rotor eccentricity due to machining or operating force imbalance to assess pressure pulsation variations downstream of an OWC device. Therefore, an eccentric setup of the study object is required, as shown in Fig. 3. Using the center of the casing arc outside the rotor as a reference, the distance between the two centers was set as the eccentricity distance Er. Thus, there are two cases, as shown in Fig. 3 (a), wherein the two centers coincide, and the eccentricity distance Er is 0 mm. The rotor in Fig. 3 (b) is eccentric, and the eccentricity distance Er is 0.5 mm. While the rotor outer diameter is 151.5 mm, the rotor eccentricity is only 0.33%, which is a significantly small eccentricity distance.

3. PULSATION TRACKING NETWORK (PTN) METHOD

To investigate the downstream pressure pulsation in the OWC device, the pulsation tracking network (PTN) method was used in this paper (Jin et al., 2021). The PTN method was used to track the turbulent pulsation characteristics and perform a time-to-frequency conversion for the pulsation signal to obtain the relevant frequency information.

The PTN method is based on the commercial software CFX-post, which generates random point clouds of the detection surfaces of the target case and arranges a large number of monitoring points in the OWC device, constituting radial detection surfaces 1, 2, and 3 with 1000, 1000, and 1200 points, respectively, and axial downstream section detection surfaces with 6000 points. The locations of the inspection surfaces are shown in Fig. 4. Finally, the point cloud coordinates were imported into CFX-pre, and a large number of monitoring points were obtained.

Once the monitoring points were arranged, CFD numerical simulations were carried out, and the results were converted to pressure pulsation times and frequencies using fast Fourier transformation (FFT). As a periodic signal can be expressed as a sum of different sine
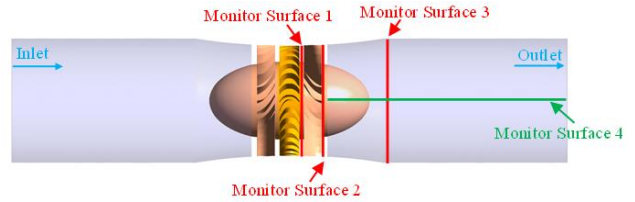

Fig. 4 Diagram of the monitor surface

(or cosine) signals, the main frequency varies, the pressure pulsation amplitude increases or decreases, and the phase change can be obtained. The sine or cosine signal with the largest amplitude dominates the original signal, and this frequency is called the dominant frequency. The pressure pulsation is dimensionless, and the pressure pulsation amplitude is defined as C_p:

$$C_p = \frac{P - \overline{P}}{\frac{1}{2}\rho V^2} \tag{1}$$

where $\overline{P}$ is the average value of the pressure pulsation at each monitoring point (Pa), and V is the average velocity at the downstream outlet section of the OWC device (m/s). We addressed the operation of OWC turbines in which common air velocities are not considered to have a dangerous effect on the devices' operation. Air noise was not considered in this study, and we will investigate the effect of noise in a subsequent study.

For a given frequency, the phase at a point is selected as the initial phase φ_0, and the phase at point k is φ_k. The phase difference $\Delta\varphi_k$ at each point at the selected frequency can be calculated using the following equation:

$$\Delta\varphi_k = \varphi_k - \varphi_0 - 2n\pi \tag{2}$$

where $\varphi_k < \varphi_0 - \pi$, $n = -1$; $\varphi_0 - \pi \leq \varphi_k \leq \varphi_0 + \pi$, $n = 0$; $\varphi_k > \varphi_0 + \pi$, $n = 1$. The values of $\Delta\varphi_k$, φ_k, and φ_0 are $-\pi \sim \pi$.

A specific analysis was carried out based on the frequencies sought to reveal the changes in the downstream flow field of the OWC device due to eccentricity.

4. SETUP OF SIMULATION

4.1 CFD Setup

Computational fluid dynamics (CFD) is an important research approach based on fluid dynamics and numerical simulation and contributes to the flow analysis and performance optimization of air machinery. This paper is based on CFD using the commercial software ANSYS CFX to simulate the fluid motion between rotor stators and analyze the downstream pressure pulsations. Therefore, the CFD setup was carried out with a fluid medium of 25°C air and a reference pressure of 1Atm. The SST k-ω model has good convergence and high stability and can simulate most turbulent states, so the SST k-ω turbulence model was chosen, with the transport equations for the turbulent kinetic energy k and specific dissipation rate ω expressed as

$$\frac{\partial(\rho k)}{\partial t}+\frac{\partial(\rho u_i k)}{x_i}=P-\frac{\rho k^{3/2}}{l_{k-w}}+\frac{\partial(\rho k)}{\partial x_i}\left[(\mu+\sigma_k\mu_i)\frac{\partial k}{\partial x_i}\right] \quad (3)$$

$$\frac{\partial(\rho\omega)}{\partial t}+\frac{\partial(\rho u_i\omega)}{x_i}=C_\omega P-\beta\rho\omega^2+\frac{\partial}{\partial x_i}\left[(\mu_l+\sigma_\omega\mu_i)\frac{\partial\omega}{\partial x_i}\right]$$
$$+2(1-F_1)\frac{\rho\sigma_{\omega2}}{\omega}\frac{\partial k}{\partial x_i}\frac{\partial\omega}{\partial x_i} \quad (4)$$

where ρ is the fluid density, P is the turbulence generation term, μ is the dynamic viscosity, μ_t is the eddy viscosity coefficient, σ is the model constant, C_ω is the coefficient of turbulent dissipation term, and F_1 is the blending equation. A hybrid of the k-ε and k-ω modes is made according to the flow zone.

In the calculation domain, the inlet of the OWC device was set to a velocity-inlet-type boundary condition with a velocity of V_a, and the outlet was set to a hydrostatic-outlet-type boundary condition with a pressure value of 0 Pa. All walls were set to slip-free walls and a multi-reference frame (MRF) model was used, with the rotor set to a rotational reference system with a speed of 150 rad/s. The rest of the components were set to a static reference system. The General Grid Interface (GGI) model was chosen for the data transfer between the different components.

Numerical simulation performs steady and unsteady calculations, using the steady calculation results as the initial file for the unsteady calculations. The convergence criterion is determined based on the root-mean-square residuals of the momentum and continuity equations being less than 0.0001.

4.2 Grid Preparation and GCI Check

Mesh delineation plays a vital role in CFD simulations and therefore must be delineated and checked for irrelevance before numerical simulations can be carried out. In this paper, the core components of the OWC device, the rotor and stator, consisted of hexahedral cells, and the inlet and outlet pipe sections consisted of tetrahedral cells. Figure 5 shows the computational domain and mesh for the CFD simulation, and Table 1 illustrates the number of mesh nodes for each component. In addition, in this study, the wall y+ values of the various overflow components were all between 10 and 100 to facilitate the application of the wall function.

To balance the calculation time and accuracy, the mesh accuracy was checked using the "mesh convergence index" method. Three sets of meshes were chosen, with the number of meshes in multiples, namely, fine, medium, and coarse. Using the efficiency η of the OWC device as an objective function, the variation in η is shown in Fig. 6. This method was based on the Richardson extrapolation method with mesh refinement factors of 1.339 and 1.306. The mesh convergence index was verified to be 0.416% for the medium and fine meshes and 3.59% for the medium and coarse meshes. According to the calibration results, the medium grid had the advantages of fast convergence and high calculation accuracy with 112 million nodes (see Table 1) so the medium grid was chosen as the final calculation grid.
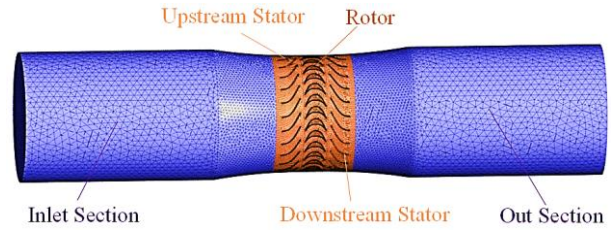

Fig. 5 Fluid domain and mesh for CFD simulation

Table 1 Number of grid nodes for each component of the OWC device

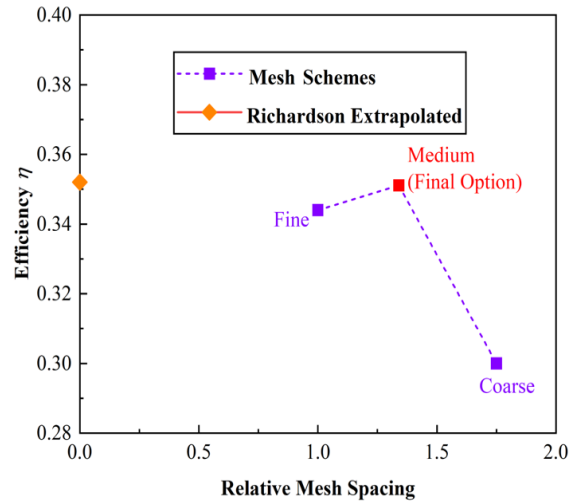| Part name	Number of grid nodes
Inlet section	0.79×10^5 nodes
Upstream stator	2.37×10^5 nodes
Rotor	4.85×10^5 nodes
Downstream stator	2.37×10^5 nodes
Outlet section	0.79×10^5 nodes

Fig. 6 Convergence index check of mesh

5. PERFORMANCE COMPARISON

In the process of fitting the numerical simulation to the experimental results, seven different flow coefficient φ moments were selected and fitted with the OWC device efficiency η as the objective function, and the performance of the device before eccentricity was close to the experimental performance, as shown in Fig. 7. The flow coefficient φ is defined as

$$\varphi=\frac{V_a}{U_r} \quad (5)$$

where V_a is the inflow velocity, and U_r is the rotational linear velocity at the mid-span of the rotor.

In Fig. 7, the performance curve of the OWC device with rotor eccentricity is not significantly different from that with non-eccentricity or the experimental data curve. Therefore, it can be concluded that the rotor producing a small distance eccentricity has a small effect on the performance of the OWC device, and no direct change in performance can be seen. Therefore, this paper used the
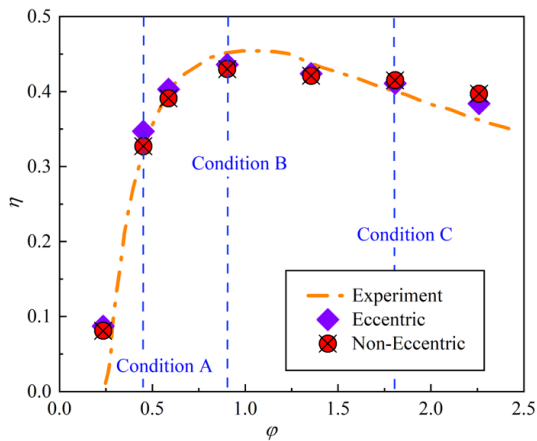
Fig. 7 Comparison of efficiency η between simulation data and experimental data (Setoguchi et al., 2004)

(a) Condition A—Non-Eccentric

(b) Condition A—Eccentric

(c) Condition B—Non-Eccentric

(d) Condition B—Eccentric

(e) Condition C—Non-Eccentric
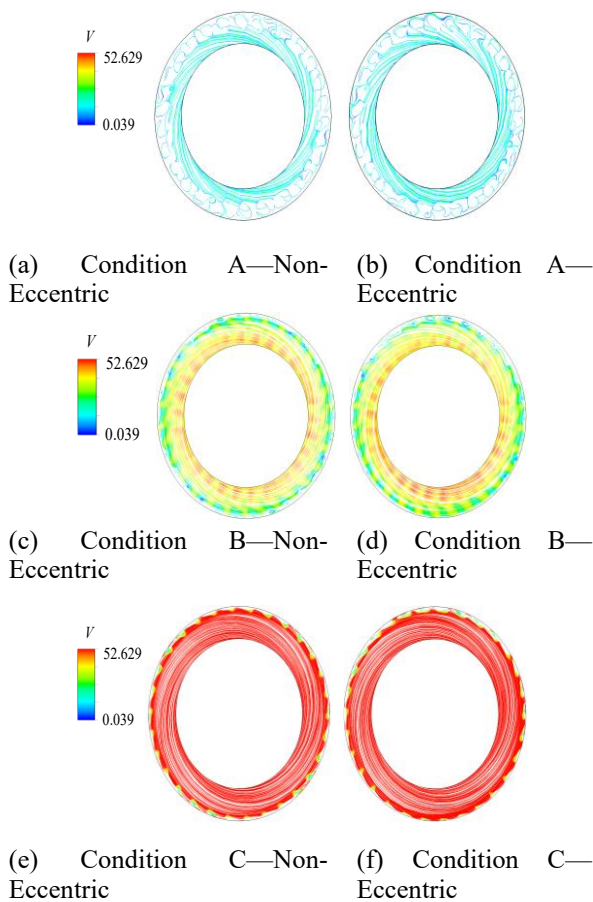
(f) Condition C—Eccentric

Fig. 8 Comparison of flow fields on monitor surface 1

PTN method to analyze the eccentric rotor in an attempt to directly reveal the details of how the OWC device is affected by eccentricity.

6. COMPARATIVE ANALYSIS

6.1 Flow Field Comparison

Three typical operating conditions have been selected from Fig. 7: Condition A—low-flow condition, Condition C—high-flow condition, and Condition C—high-flow
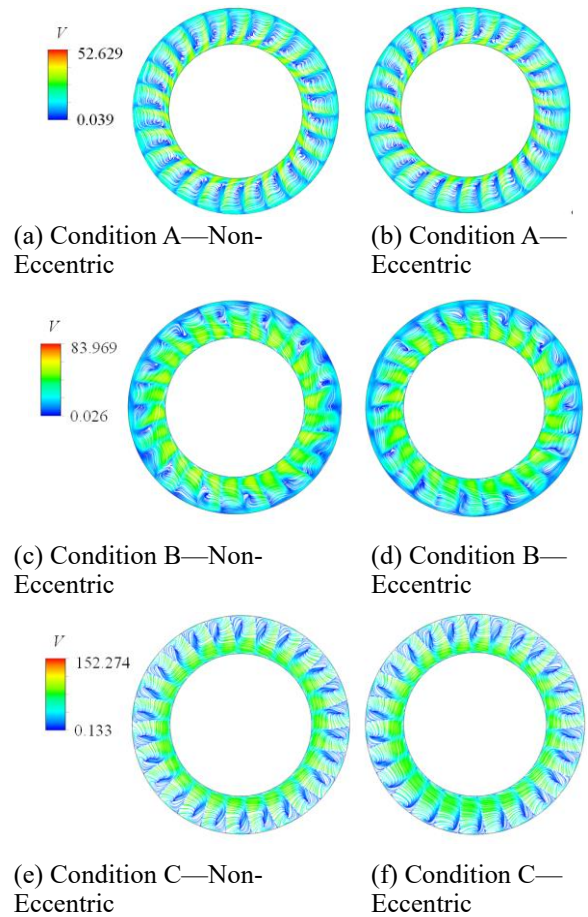

(a) Condition A—Non-Eccentric

(b) Condition A—Eccentric

(c) Condition B—Non-Eccentric

(d) Condition B—Eccentric

(e) Condition C—Non-Eccentric

(f) Condition C—Eccentric

Fig. 9 Comparison of flow fields on monitor surface 2.

condition. The flow line diagrams of velocity V in the flow field at different detection surfaces were created and are shown. Figure 8 (a)(b) shows that under Condition A, there is no significant change in the flow field streamlines between the rotor being eccentric and non-eccentric, with vortices present on both sides near the shell and uniformly present on the rotor shaft side. In (c) (d), it can be seen that after the rotor is eccentric, the flow velocity on the eccentric side significantly increases, by approximately 50%, and some vortices are generated on the opposite side. In (e) (f), it is also evident that the flow velocity on the eccentric side increases by approximately 30% and that the vortices increase on the symmetrical side. From the above phenomena, it can be judged that the eccentricity leads to enhanced blade tip leakage, and the blade tip leakage meets the mainstream, causing an increase in vortices.

Figure 9 (a)(b) shows that in Condition A, there is no significant change in the flow line between the rotor being eccentric and non-eccentric, and the fluid flow is relatively constant. In (c) (d), it can be seen that after the rotor is eccentric, the flow velocity increases on the eccentric side by approximately 25%. In (e) (f), it can be seen that the flow velocity on the eccentric side significantly increases. Vortices are present in both cases, with the vortex on the eccentric side being significantly larger than on the non-eccentric side. On monitor surface 2, the rotor is eccentric, and there is a slight change in the flow line and a tendency for the vortices to increase. However, this is not very obvious.
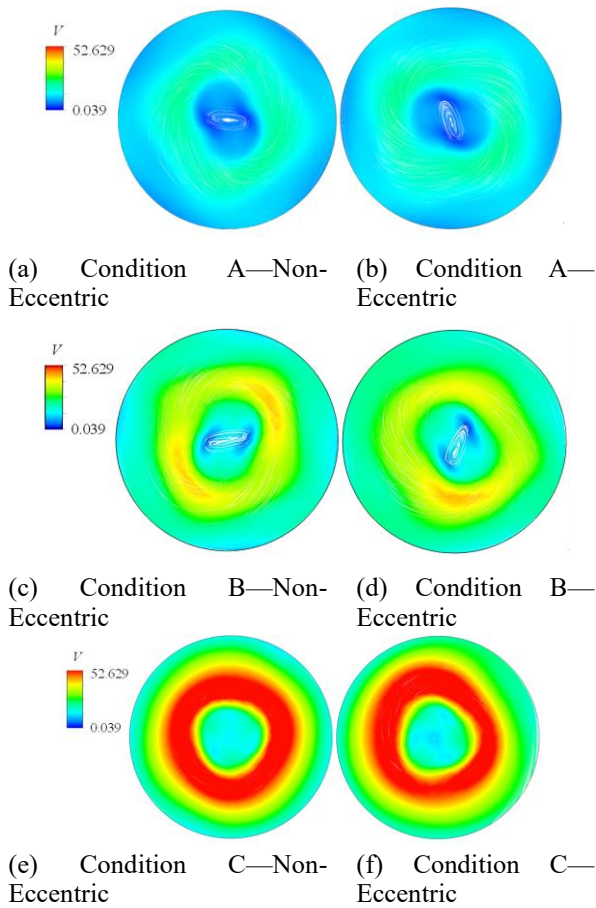
(a)   Condition   A—Non-Eccentric   (b) Condition A—Eccentric

(c)   Condition   B—Non-Eccentric   (d) Condition B—Eccentric

(e)   Condition   C—Non-Eccentric   (f) Condition C—Eccentric

Fig. 10 Comparison of flow fields on monitor surface 3

(a) Condition A—Non-Eccentric

(b) Condition A—Eccentric

(c) Condition B—Non-Eccentric

(d) Condition B—Eccentric

(e) Condition C—Non-Eccentric

(f) Condition C—Eccentric

Fig. 11 Comparison of flow diagrams on monitor surface 4

Figure 10 (a)(b) demonstrates that under Condition A, there is no significant change in the flow field streamlines between the rotor eccentricity and non-eccentricity, and the fluid flow is relatively steady. However, it can be seen that the direction of fluid rotation is deflected. In (c) and (d), it can be seen that the deflection angle of the direction of rotation increases after the rotor is eccentric. The velocity of the flow without rotor eccentricity is a symmetrical distribution, while the velocity of the eccentric side increases and that of the opposite side decreases after eccentricity. In (e) and (f), it can be seen that after the rotor is eccentric, the velocity on the eccentric side increases. Before the rotor becomes eccentric, the high-speed area is circular. After the rotor is eccentric, the shape of the high-speed area is deformed, showing an imbalance between the velocities on both sides.

Figure 11(a)(b) shows the flow field flow diagram for monitor surface 4, where it can be seen that there is no significant change in the streamline from non-eccentricity to rotor eccentricity at low flow rates in Condition A. However, the vortex on the side near the shell becomes more turbulent after the rotor is eccentric. (c) and (d) reveal that the vortices generated in the downstream outlet section are symmetrical when the rotor is non-eccentric, whereas the vortices generated in the downstream outlet show an asymmetrical situation and tend to increase after the rotor is eccentric. However, there is no significant
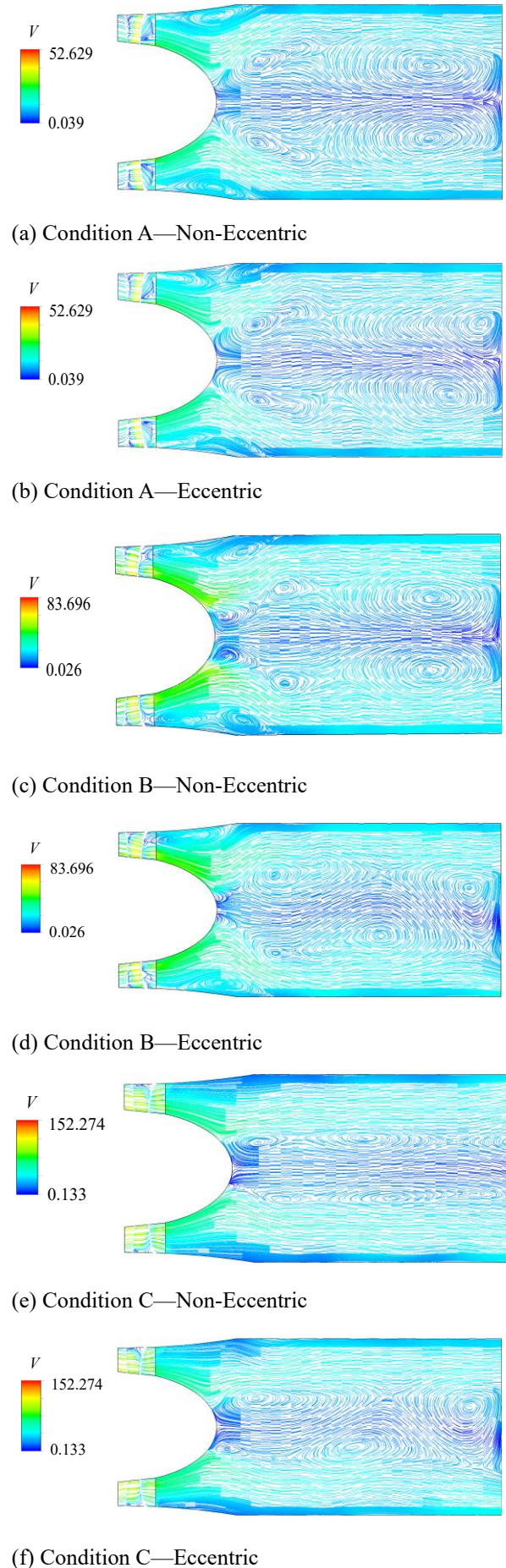
a) Condition A—Non-Eccentric

b) Condition A—Eccentric

c) Condition B—Non-Eccentric

d) Condition B—Eccentric

e) Condition C—Non-Eccentric
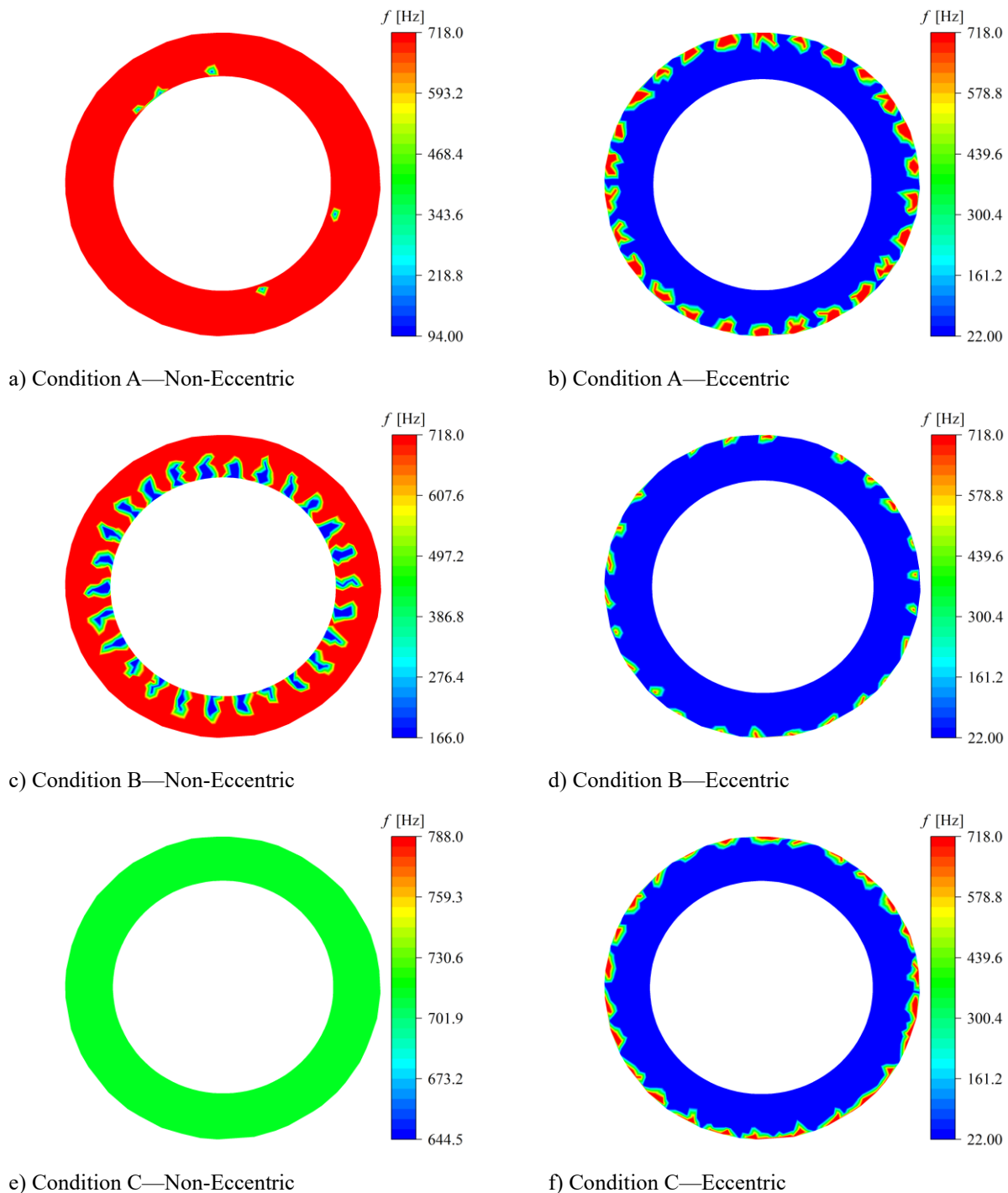

f) Condition C—Eccentric

Fig. 12 Comparison of main frequencies on monitor surface 1

change in the flow field velocity in both cases, and the flow lines are relatively uniform. (e) and (f) show a situation similar to that for Condition B. Therefore, we judge that the change in the flow rate does not affect the change in the flow velocity in the outlet section, but it affects the number and size of the vortices generated.

6.2 Main Frequency Comparison

Figure 12 compares the frequency distributions of the eccentric and non-eccentric rotor under different operating conditions at different monitor surfaces with a blade frequency of 716.1972Hz and rotation frequency of 23.8732Hz.

As can be seen in Fig. 12 (a) (b), in the non-eccentric

condition A, the pressure pulsation on monitor surface 1 is dominated by the 1-time blade frequency, and when the rotor is eccentric, the dominant frequency of the pressure pulsation is converted from the 1-time blade frequency to the 1-time rotation frequency and is locally dominated by the 1-time blade frequency, mixed with the 0.5-times blade frequency. (c) and (d) show that in Condition B without rotor eccentricity, the pressure pulsation on monitor surface 1 is mostly dominated by the 1-time blade frequency and locally by the 7-times rotation frequency and 0.5-times blade frequency. After the rotor is eccentric, the majority of the pressure pulsation on monitor surface 1 is dominated by the 1-time rotation frequency, with a very small proportion dominated by the 1-time blade
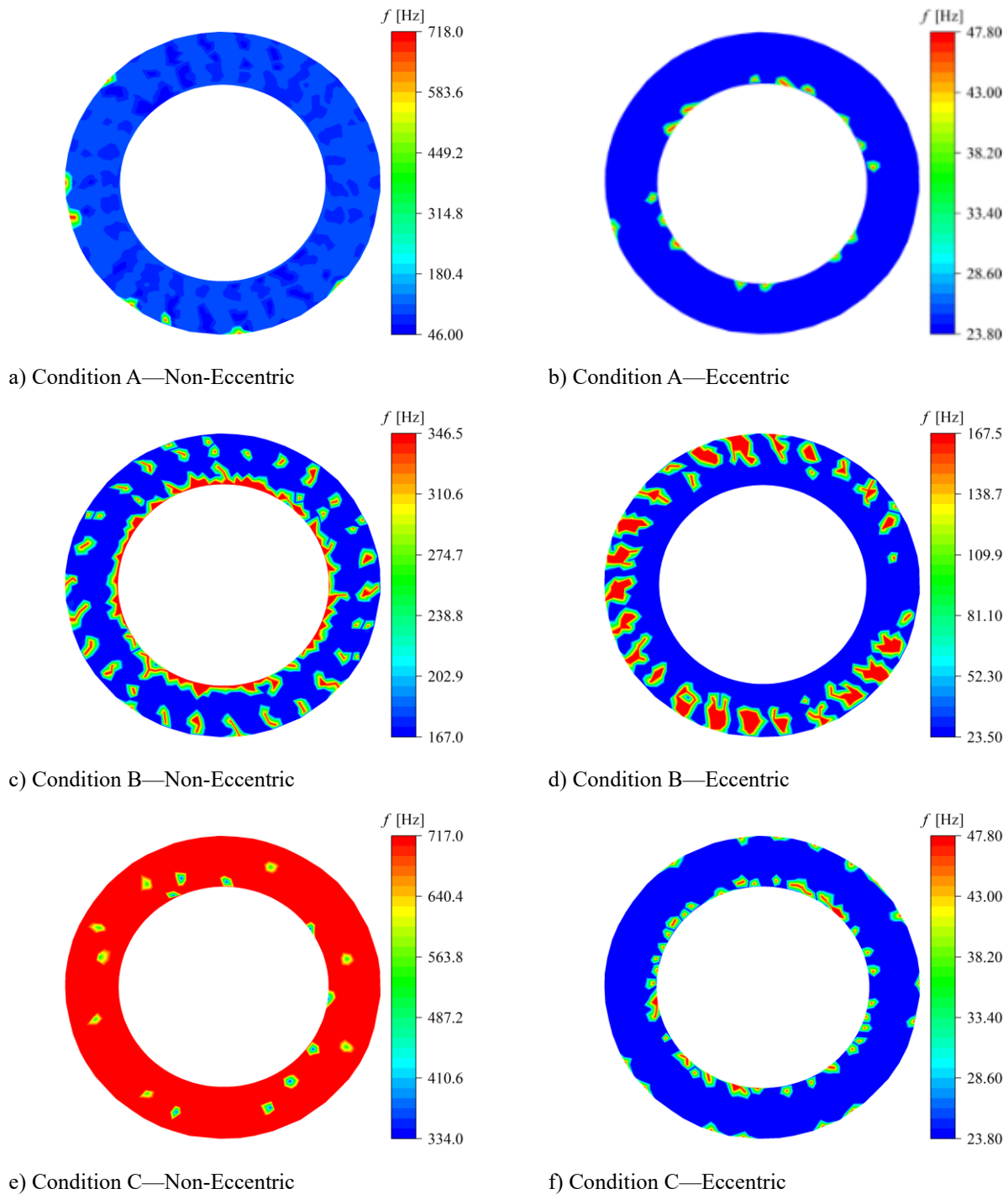
a) Condition A—Non-Eccentric

b) Condition A—Eccentric

c) Condition B—Non-Eccentric

d) Condition B—Eccentric

e) Condition C—Non-Eccentric

f) Condition C—Eccentric

Fig. 13 Comparison of main frequencies on monitor surface 2

frequency. (e) and (f) show that in Condition C, the rotor is non-eccentric, and the pressure pulsation on monitor surface 1 is completely dominated by the 1-time blade frequency, and after eccentricity, the pressure pulsation on the monitor surface 1 is mostly dominated by the 1-time rotation frequency, with a small part dominated by the 1-time blade frequency.

As can be seen in Fig. 13 (a) (b), in the non-eccentric condition A, the pressure pulsation is almost dominated by the 15-times rotation frequency. When the rotor is eccentric, the pressure pulsation is almost completely dominated by the 1-time rotation frequency. (c) and (d) show that in Condition B without rotor eccentricity, the

pressure pulsations on monitor surface 2 are mostly dominated by the 7-times rotation frequency and locally by the 15-times rotation frequency. After the rotor is eccentric, the dominant frequency of the pressure pulsation on monitor surface 2 tends to decrease and, for the most part, is dominated by the 1-time rotational frequency and locally by the 7-times rotation frequency. (e) and (f) show that in Condition C without rotor eccentricity, almost all of the pressure pulsation on monitor surface 2 is dominated by the 1-time blade frequency. After eccentricity, most of the pressure pulsation on monitor surface 2 is dominated by the 1-time rotation frequency, with a small proportion dominated by
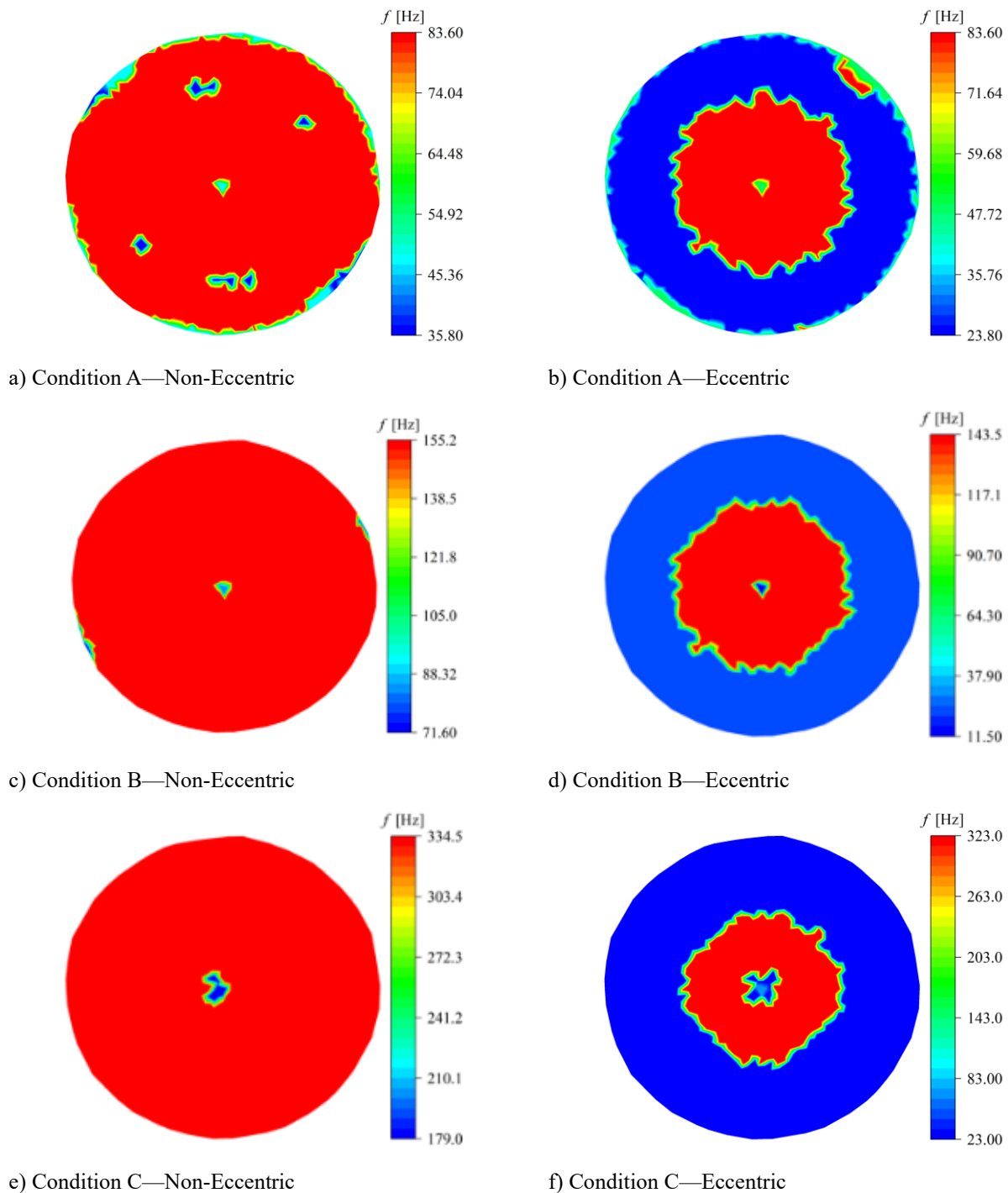
a) Condition A—Non-Eccentric

b) Condition A—Eccentric

c) Condition B—Non-Eccentric

d) Condition B—Eccentric

e) Condition C—Non-Eccentric

f) Condition C—Eccentric

Fig. 14 Comparison of main frequencies on monitor surface 3

the 2-times rotation frequency.

As can be seen in Fig. 14 (a) (b), in the non-eccentric condition A, the pressure pulsations on monitor surface 3 are dominated by the approximately 3.6-times rotation frequency. When the rotor is eccentric, the pressure pulsation is dominated mostly by the 1-time rotation frequency and locally by the 3.6-times rotation frequency. (c) and (d) show that in Condition B without rotor eccentricity, the pressure pulsation on monitor surface 3 is mostly dominated by the 7-times rotation frequency. After the rotor is eccentric, most of the pressure pulsation on monitor surface 3 is dominated by the 1-time rotation frequency and locally by the 6-times rotation frequency.

(e) and (f) show that under Condition C without rotor eccentricity, almost all the pressure pulsation on monitor surface 3 is dominated by the 0.5-times blade frequency. After eccentricity, most of the pressure pulsation on monitor surface 3 is dominated by the 1-time rotation frequency and locally dominated by the 0.5-times blade frequency.

6.3 Phase Change

Figure 15 shows that the phase change direction in different operating conditions is consistent with the direction of fluid motion with rotor eccentricity and non-eccentricity. However, comparing the phase change for
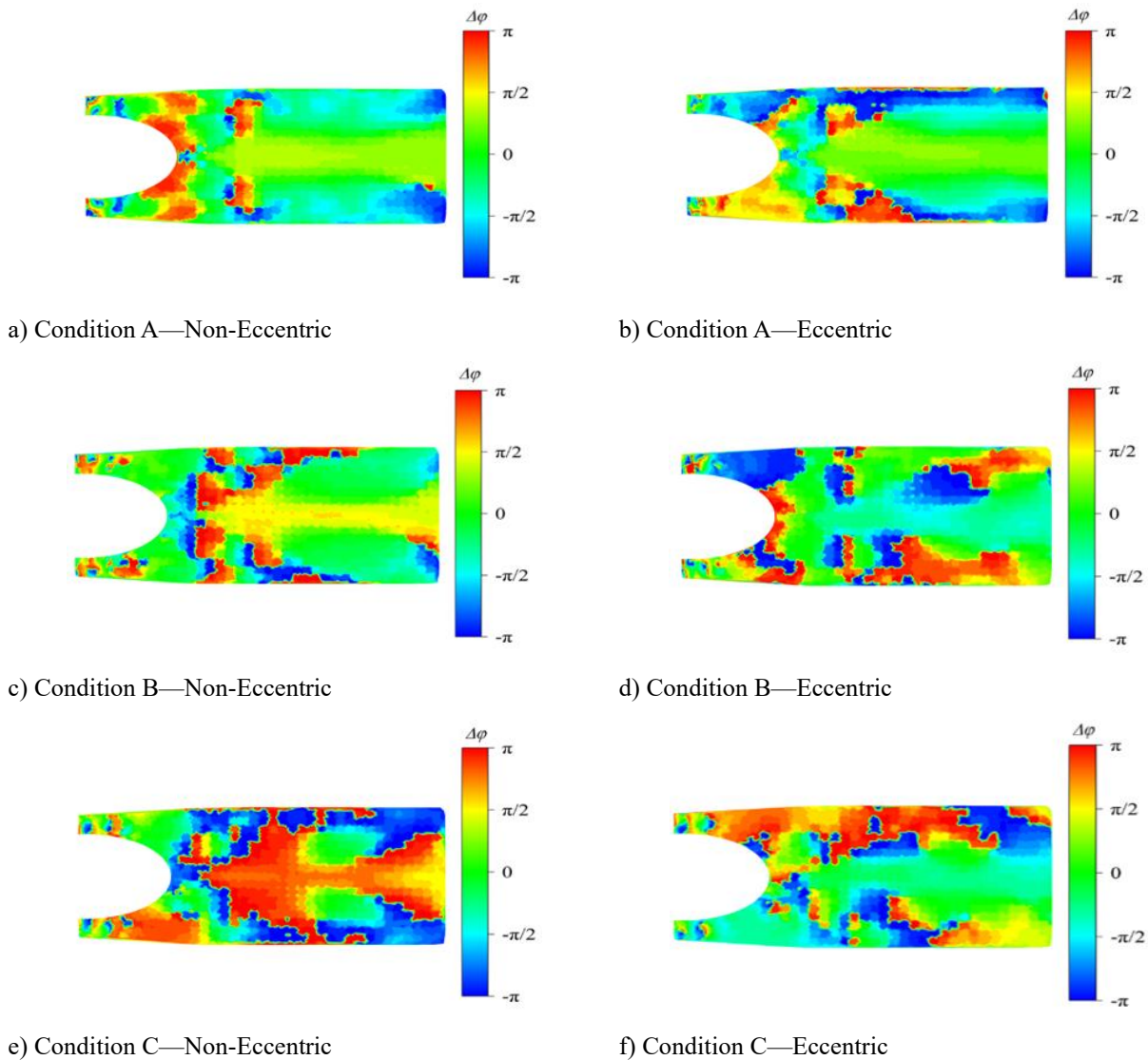
a) Condition A—Non-Eccentric

b) Condition A—Eccentric

c) Condition B—Non-Eccentric

d) Condition B—Eccentric

e) Condition C—Non-Eccentric

f) Condition C—Eccentric

Fig. 15 Comparison of phase changes on monitor surface 4

the eccentric and non-eccentric cases under the same operating conditions, it can be found that the phase change diagram for the non-eccentric rotor is approximately. symmetrical about the rotational axis of the OWC device, while the phase change diagram for the eccentric rotor does not have a clear symmetrical relationship. Therefore, it is judged that rotor eccentricity affects the wave's steady propagation.

6.4 Pressure Pulsation Amplitudes Comparison

Figure 16 reveals the pressure pulsation amplitudes on monitor surface 4 for the OWC device under three typical operating conditions with a 1-time blade frequency intensity. The pressure pulsation amplitude on monitor surface 4 does not significantly change between the non-eccentric and the eccentric rotor. Therefore, it is judged that a small rotor eccentricity distance at a 1-time blade frequency has a small effect on the downstream pressure pulsation amplitude.

Figure 17(a) (b) shows that at a 1-time rotation frequency intensity, before the rotor is non-eccentric under Condition A, the pressure pulsation amplitude

downstream of the monitor surface is small. After eccentricity, the downstream pressure pulsation amplitude increases abruptly to approximately 10 times the pressure pulsation amplitude's magnitude without the rotor being eccentric. (c) and (d) shows that in Condition B, before the rotor is eccentric, the pressure pulsation amplitude downstream of the monitor surface is very small, whereas after the rotor is eccentric, the pressure pulsation amplitude increases sharply and is approximately 10 times greater than before the rotor is eccentric, concentrated at the downstream rotor outlet and the downstream guide vane outlet. (e) (f) shows that in Condition C, when the rotor is non-eccentric, the pressure pulsation amplitude is mainly concentrated behind the downstream guide vane outlet, but the pressure pulsation amplitude is smaller. After the rotor is eccentric, the pressure pulsation amplitude increases sharply and covers almost the whole flow passage, and only the pressure pulsation amplitude behind the downstream guide vane outlet is relatively small. From the above, it can be judged that the influence of rotor eccentricity on the pressure pulsation amplitude downstream of the OWC device tends to increase gradually as the working flow rate increases.
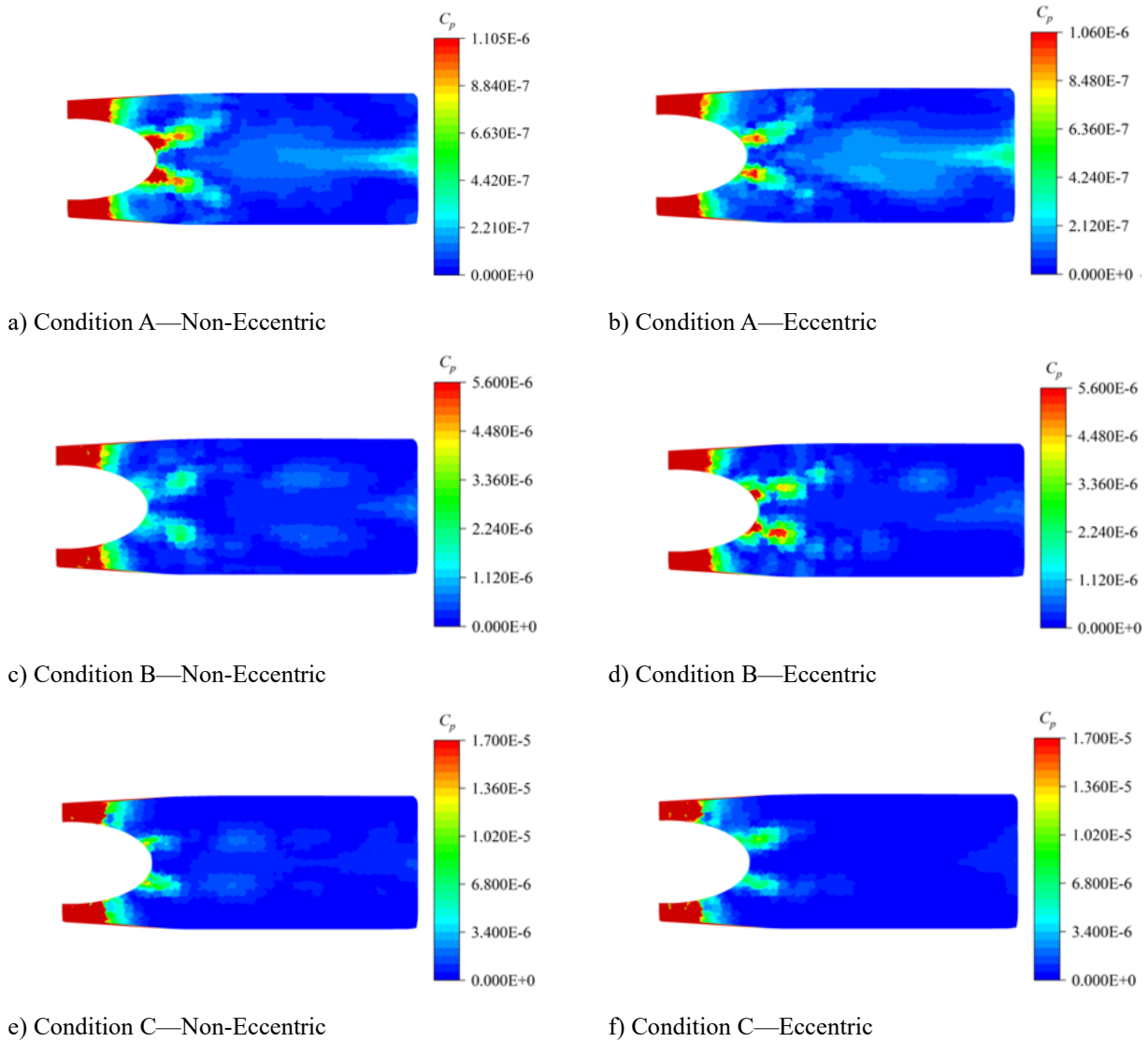
a) Condition A—Non-Eccentric

b) Condition A—Eccentric

c) Condition B—Non-Eccentric

d) Condition B—Eccentric

e) Condition C—Non-Eccentric

f) Condition C—Eccentric

Fig. 16 Pressure pulsation amplitudes on monitor surface 4 at 1-time blade frequency

7. CONCLUSIONS

This paper focused on the variation in the downstream pressure pulsations of an OWC device's rotor under eccentric and non-eccentric conditions. The following conclusions were drawn.

The dominant downstream pressure pulsation frequency in the OWC device was influenced by different operating conditions, different monitor surfaces, and whether the rotor was eccentric or not. The exact dominant frequency needed to be analyzed in detail, where most of the pressure pulsation on the non-eccentric was dominated by the 1-time blade frequency, and most of the pressure pulsation on the eccentric monitor surface 1 was dominated by the 1-time rotation frequency. For the remaining flow conditions, the dominant frequency varied between the 1-time blade and rotation frequency in the eccentric and non-eccentric cases. The main dominant frequencies were the 2-times, 3.6-times, 6-times, and 7-times rotation frequencies, and the 0.5-times blade frequency. Regarding the pressure pulsation amplitude after the time-to-frequency conversion, there was no significant change in the pressure pulsation amplitude

between the eccentric and non-eccentric OWC device at a 1-time blade frequency intensity. In contrast, the pulsation amplitude increase significantly at the 1-time rotation frequency intensity, with the pressure pulsation amplitude of the eccentric rotor being approximately 10 times greater than that of the non-eccentric rotor under low- and high-efficiency-flow conditions, and the pressure pulsation amplitude region with the eccentric rotor being 200 times greater than that of the non-eccentric rotor under high-flow conditions, which is concerning. Regarding phase change, the direction of phase change was consistent with the direction of fluid movement. Before eccentricity, however, the phase change trend was symmetrical about the axis of rotation. After the rotor was eccentric, the phase change trend became gradually disordered, showing no obvious trend. Therefore, it is judged that rotor eccentricity interferes with the stability of the pressure pulsation's phase change.

Combining time-to-frequency conversion with CFD numerical simulations, the pulsation tracking network (PTN) method is superior to the traditional pressure pulsation monitoring point method. Conveniently, the PTN method is based on a large number of monitoring points and can reveal the details of the dominant frequency
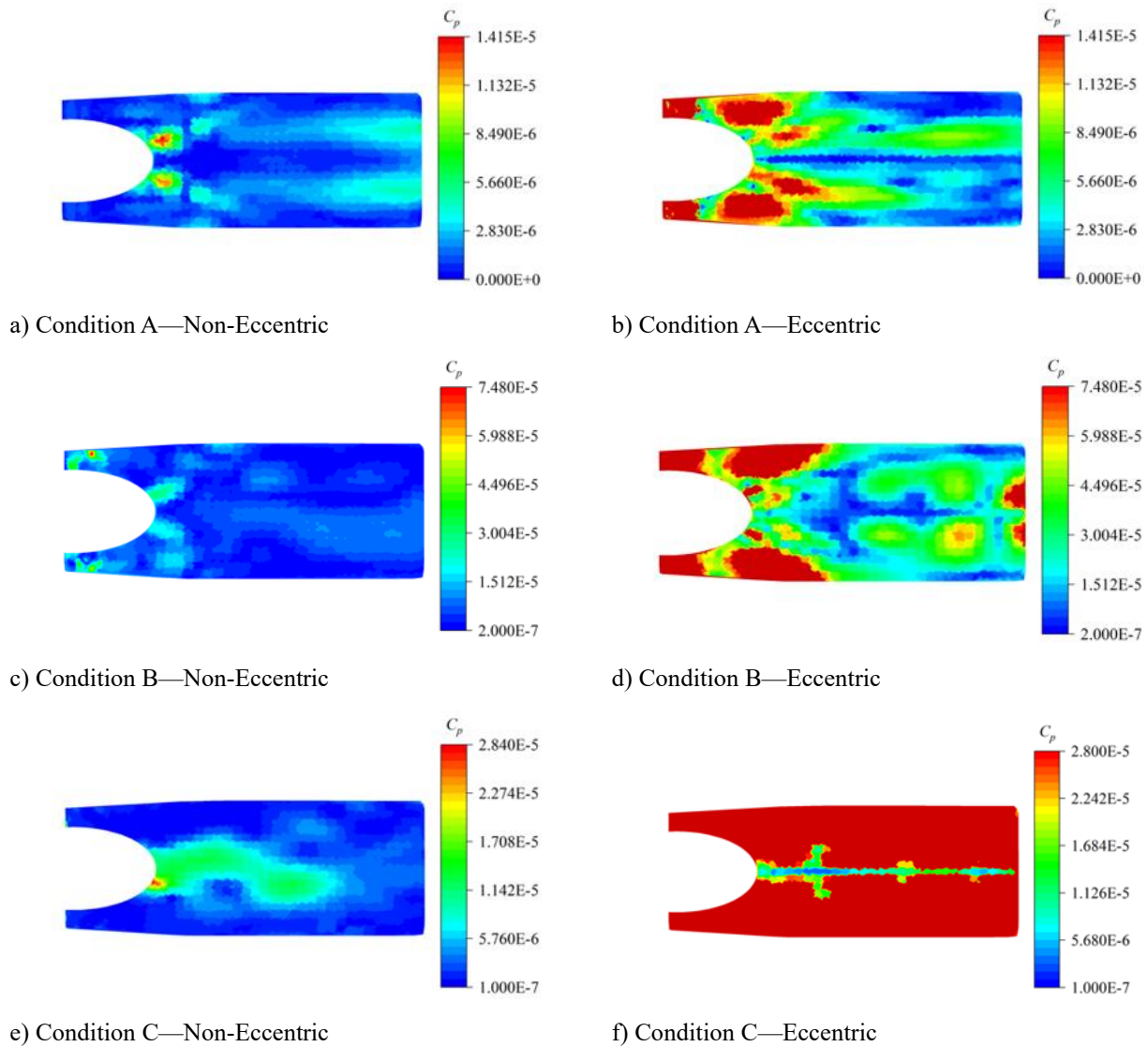
a) Condition A—Non-Eccentric

b) Condition A—Eccentric

c) Condition B—Non-Eccentric

d) Condition B—Eccentric

e) Condition C—Non-Eccentric

f) Condition C—Eccentric

Fig. 17 Pressure pulsation amplitude on monitor surface 4 at 1-time rotation frequency

change process, the increase or decrease in the pressure pulsation amplitude, and the phase change. Analysis using this method elucidates the effect of eccentricity on downstream pressure pulsations and flow fields, thus guiding vibration analysis and reduction during device operation.

ACKNOWLEDGEMENTS

CONFLICT OF INTEREST

The authors declare that they have no known competing financial interests or personal relationships that could have appeared to influence the work reported in this paper.

AUTHOR CONTRIBUTION

All authors contributed to the study conception and design. The numerical analyses were conducted by both **J. H. Lu** and **Q. Liu**; The paper was written by **J. H. Lu**; The project was initiated and the paper edited by **F. Y. Jin**; The numerical analyses and paper drafting was assisted by **D. Zhu**; The whole project was guided and organized by **R. Tao** and **R. F. Xiao**; All authors commented on previous versions of the manuscript. All authors read and approved the final manuscript

REFERENCES

Bao, X. H., Li, F. Y., Fang, Y., et al. (2015). Sub-critical speed vibration of rotors for large submersible motors with mixed eccentricity. *Transactions of China Electrotechnical Society*, *30*(6), 142-149.

Bell, D. L., & He, L. (2000). Three-dimensional unsteady flow for an oscillating turbine blade and the influence of tip leakage. *Journal of Turbomachinery-Transactions of the ASME*, *122*(1), 93-101. https://doi.org/10.1115/1.555432

Decaix, J., Dreyer, M., Balarac, G., et al. (2018). RANS computations of a confined cavitating tip-leakage vortex. *European Journal of Mechanics B-Fluids*, *67*, 198-210.

https://doi.org/10.1016/j.euromechflu.2017.09.004

Eric T. D., Shawn S., Reid A. B., & Karen A T. (2022). Evaluating the influence of rotor-casing eccentricity on turbine efficiency including time-resolved flow field measurements. *Journal of Turbomachinery-Transactions of the Asme*, *144*(2). https://doi.org/10.1115/1.4052318

Falcao, A. F. O., & Henriques, J. C. C. (2016). Oscillating-water-column wave energy converters and air turbines, A review. *Renewable Energy*, *85*, 1391-1424. https://doi.org/10.1016/j.renene.2015.07.086

Gao, Z., Narzary, D. P., & Han, J. C. (2008). Film cooling on a gas turbine blade pressure side or suction side with axial shaped holes. *International Journal of Heat and Mass Transfer*, *51*(9-10), 2139-2152. https://doi.org/10.1016/j.ijheatmasstransfer.2007.11.010

Jin, F. Y., Tao, R., Lu, Z. H., Xiao, R. F. (2021). A spatially distributed network for tracking the pulsation signal of flow field based on CFD simulation. M*ethod and A Case Study. Fractal and Fractional*, *5*(4), 181. https://doi.org/10.3390/fractalfract5040181

Kamath, A., Bihs, H., & Arntsen, O. A. (2015). Numerical investigations of the hydrodynamics of an oscillating water column device. *Ocean Engineering*,*102*, 10-50. https://doi.org/10.1016/j.oceaneng.2015.04.043

Li, Y., Wu, Z. C., Tagawa Kotaro; et al. (2018). Numerical simulation on aerodynamic characteristics of vertical axis wind turbine with eccentric rotor structure. *Journal of Drainage and Irrigation Machinery Engineering*, *36*(5), 413-419.

Lu, Z. H., Li, N., Tao, R., Yao, Z. F., Liu, W. C., Xiao, R. F. (2022). Influence of eccentric impeller on pressure pulsation of large-scale vaned-voluted centrifugal pump, *Proceedings of The Institution of Mechanical Engineers Part A-Journal of Power and Energy*, *237*(3)   ,   591-601. https://doi.org/10.1177/09576509221128344

Mao, Y. J., Fang, S. Z., Li, T., et al. (2016). *Study on the vibration characteristic of turbine rotor eccentricity based on FFT.* Proceedings of 2016 7th International Conference on Mechanical and Aerospace Engineering, ICMAE, 239-243.

Miorini, R. L., Wu, H. X., & Katz, J. (2012). The internal structure of the tip leakage vortex within the rotor of an axial waterjet pump. *Journal of Turbomachinery-Transactions of the ASME*, *134* (3). https://doi.org/10.1115/1.4003065

Pelc, R., & Fujita, R. M. (2002). Renewable energy from the ocean. *Marine Policy*, *26* (6), 471-479. https://doi.org/10.1016/S0308-597X(02)00045-3

Peters, R., Lundin, U., & Leijon, M. (2007). Saturation effects on unbalanced magnetic pull in a hydroelectric generator with an eccentric rotor. *IEEE Transactions on Magnetics*, *43*(10), 3884-3890. https://doi.org/10.1109/TMAG.2007.903275

Rehder, H. J., & Dannhauer, A. (2007). Experimental investigation of turbine leakage flows on the three-dimensional flow field and endwall heat transfer. *Journal of Turbomachinery-Transactions of the ASME*,   *129*(3),   608-618. https://doi.org/10.1115/1.2720484

Setoguchi, T., Takao, M., Santhakumar, S., & Kaneko, K. (2004). Study of an impulse turbine for wave power conversion, effects of Reynolds number and hub-to-tip ratio on performance. *Journal of Offshore Mechanics and Arctic Engineering*, *126*(2), 137-140. https://doi.org/10.1115/1.1710868

Simshauser, P. (2022). Fuel poverty and the 2022 energy crisis. *Australian Economic Review, 55*(4), 503-514. https://doi.org/10.1111/1467-8462.12492

Sinha, B. K. (2002). Trend prediction from steam turbine responses of vibration and eccentricity. Proceedings of the institution of mechanical engineers, part A. *Journal of Power and Energy*, *216*(1), 97-103. https://doi.org/10.1243/095765002760024872

Venter, S. J., & Kroger, D. G. (1992). The effect of tip clearance on the performance of an axial-flow fan. *Energy Conversion and Management*, *33*(2), 89-97. https://doi.org/10.1016/0196-8904(92)90094-D

Volokhovskaya, O. A., & Barmina, O. V. (2016), Effect of initial bending and residual eccentricity of a turbine rotor on its transient vibration amplitudes. *Journal of Machinery Manufacture and Reliability, 45*(2), 113-121. https://doi.org/10.3103/S1052618816020151

Wang, H. M., Wu, Y. Z., Wang, X. H., Hu, Z. L., Lei, X. C., Yang, X. L., Zhu, D., Tao, R., Xiao, R. F. (2022). Influence of runner eccentricity on the hydraulic performance of tubular turbine, a comparative case study. *Proceedings of the Institution of Mechanical Engineers Part A-Journal of Power and Energy, 237*(4),   819-830. https://doi.org/10.1177/09576509221137631

Wang, J. X., Yang, A. L., Li, G. P., et al, (2014a). Effect of non-uniform tip clearance on the flow exciting force in axial pump. *Journal of Engineering Thermophysics*, *35*(10), 1973-1978.

Wang, X. L., Ge, B. M., Ferreira, FJTE (2014b). Radial force analytic modeling for a novel bearingless switched reluctance motor when considering rotor eccentricity. *Electric Power Components and Systems*, *42*(6), 544-553. https://doi.org/10.1080/15325008.2014.880968

Wang, Y. B. (2004). Shaft mis-alignment induced vibration in high-capacity steam-turbine generator sets. *Power Engineering*, *24*(6), 768-774, 784.

Yu, T., Shuai, Z. J., Jian, J. X. (2022). Numerical study on hydrodynamic characteristics of a centrifugal pump influenced by impeller-eccentric effect. *Engineering Failure   Analysis*,   *138*. https://doi.org/10.1016/j.engfailanal.2022.106395